ORIGINAL ARTICLE

CrossMark

Strain analysis near the cutting edge in orthogonal cutting of hinoki (*Chamaecyparis obtusa*) using a digital image correlation method

Yosuke Matsuda[1] · Yuko Fujiwara[2] · Yoshihisa Fujii[2]

Abstract

A digital image correlation (DIC) method was utilized to measure strain distributed within approximately 0.5 mm of the cutting edge during slow-speed orthogonal cutting of air-dried hinoki (*Chamaecyparis obtusa*), to clarify the relationships of the strain distribution and cutting conditions, including cutting angle (θ) and depth of cut (d). The strain was measured in 0.04 mm steps, and the measurable minimum strain was approximately 0.08%. Tensile strain of 3% or larger normal to the cutting direction, ε_y, tended to extend 0.2 mm or further ahead of the tool when $\theta \leq 60°$ and $d \geq 0.1$ mm. This tensile ε_y corresponded to the occurrence of the fore-split in Chip Type I. The tensile ε_y detected along the path of the cutting edge decreased as θ and/or d decreased. Positive shear strain, γ_{xy}, tended to be detected ahead of the tool in Type I. Negative γ_{xy} tended to be detected ahead of the tool in Type II and III ($\theta \geq 70°$, $d \geq 0.05$ mm). These γ_{xy} values were considered to be related to the elongation and shrinkage of the chip. The study confirmed the usability of the DIC method for the evaluation of cutting conditions and also to classify chip formation into chip types.

Keywords Orthogonal cutting · Digital image correlation · Chip type

Introduction

In wood cutting processes, the cutting tool applies a cutting force to the workpiece, to remove a part of the workpiece as a chip. When the cutting force is applied, stress is distributed near the cutting edge. Destruction occurs when the local stress near the cutting edge exceeds the mechanical strength of that region. As a result, a chip is produced. The strain distribution near the cutting edge, which is calculated from the stress and the modulus of elasticity, varies depending on the cutting condition, such as depth of cut or cutting angle, and also by the strength and the anisotropy of wood.

✉ Yosuke Matsuda
  yosukem@ffpri.affrc.go.jp

[1] Forestry and Forest Products Research Institute, 1 Matsunosato, Tsukuba, Ibaraki 305-8687, Japan

[2] Graduate School of Agriculture, Kyoto University, Kitashirawakaoiwake-cho, Sakyo-Ku, Kyoto, Kyoto 606-8502, Japan

Therefore, the stress and the resultant strain distribution are deeply related to the process of split, failure, and removal of the chip.

There are three types of strain that characterize chip formation. The first strain is the strain parallel to the cutting direction, which is distributed ahead of the cutting edge. For instance, there should be compression strain parallel to the cutting direction in the part of the workpiece that will be removed as a chip. The second one is the strain normal to the cutting direction distributed in the same region as the first strain; this strain is closely related to the split and removal of the chip. The third one is the shear strain distributed along the plane almost normal to the rake face; this strain is related to the chip formation accompanied by a series of shear failures. Each strain should be controlled, so as not to be excessively large. As a result, the split and failure of the chip should always take place along the path of the cutting edge. To optimize cutting conditions and minimize strain, the relationships of the cutting conditions and the machinability of wood to the strain distribution near the cutting edge need to be clarified.

Some previous studies have measured stress/strain distribution near the cutting edge in the wood cutting process. For instance, the photo elastic coating method [1, 2]

have been used for the measurement of stress/strain in the orthogonal cutting of wood. However, the coating used in those studies tended to peel off from the wood surface and failed to track the behavior of wood during the cutting. Grid patterns printed on the surface of the workpiece [3–5] have been also used for the measurement of stress/strain in the orthogonal cutting of wood. However, time-consuming preparations of the specimen are needed to apply these methods. Other studies also numerically analyzed the stress distribution in the cutting process [6–12]. However, such numerical analysis tended to be complicated when the anisotropy of wood was taken into consideration.

Instead of using those methods, we decided to utilize a digital image correlation (DIC) method [13–17], a non-contact strain measurement technique that is becoming popular in the study of wood and wood-based materials [18–23]. In the DIC method, the random speckle pattern of the digital image of the specimen is analyzed so that the preparation of specimen surface can be omitted [16, 17]. In our previous study [23], a DIC method was utilized to investigate the residual strain beneath the wood surface finished by orthogonal cutting. The study clarified the relationships of the residual strain beneath the finished surface to the cutting angle and depth of cut. The study also suggested that the DIC method may be applicable for measuring strain distribution in wood cutting processes. However, the previous study did not focus on strain related directly to chip formation.

On the other hand, the relationships of cutting conditions to the quality of chips and the finished surface [24–27], and to cutting resistance [28, 29] have been investigated from the viewpoint of chip type [24–26]. In these studies, chip formation in orthogonal cutting parallel to the grain was categorized according to the appearance of the split, failure, and removal of the chip. The relationships between numerically analyzed stress distribution and chip type have also been investigated [6, 7]. We have evaluated the deformation and quality of subsurface cell layers in wood cutting using an X-ray computed tomography (CT) system, and investigated the relationships of CT images to chip type and the mechanism of chip formation [30]. However, the strain distribution near the cutting edge and its relationships among chip types have not yet been clarified.

The purpose of this study was to clarify the effect of cutting conditions, such as cutting angle and depth of cut, on the strain distribution near the cutting edge and chip formation. Slow-speed orthogonal cutting of hinoki (*Chamaecyparis obtusa*) was conducted, and the strain distributed within approximately 0.5 mm of the cutting edge was measured using the DIC method. The relationships of strain distribution among the chip types were also investigated.

Materials and methods

Specimens

The workpiece used in this study was air-dried hinoki (*Chamaecyparis obtusa*). The air-dried density was 0.38 g/cm^3, and the moisture content was 10.6%. The annual ring width was 1.1 mm. The dimensions of the workpiece were 50 mm × 5 mm × 50 mm in longitudinal (L), radial (R), and tangential (T) directions, respectively. The workpieces were collected from heartwood. To apply the DIC method, it is necessary for the workpiece to have a random speckle pattern on its surface [16, 17]. The LT surface, which was analyzed by the DIC method, was finished by a rotary planer. The fuzzy grain that appeared randomly on the surface, and also the arrangement of tracheid and ray tissue showed a random speckle pattern for applying the DIC method, so no further artificial decoration such as spraying black paint was necessary.

Cutting experiments

The LR surface of the workpiece was cut orthogonally by feeding the cutting tool toward the workpiece using a motorized linear stage (Fig. 1). The cutting edge was perpendicular, and the feeding direction was parallel to the grain. The cutting speed was constant at 5 mm/s. The cutting tool was made of high-speed steel (SKH51) with rake faces coated with 5-μm thick chromium nitride. The wedge angle of the tool varied from 25° to 75° at intervals of 10°. The clearance angle was kept constant at 5°. Therefore, the cutting angles (θ) were 30°, 40°, 50°, 60°, 70°, and 80°. Depths of cut (d) were 0.05, 0.1, 0.2, and 0.3 mm. Cutting was conducted five times for each combination of θ and d, and the workpiece was randomly exchanged each time.

The LT surface of the workpiece during cutting was recorded as a video clip using a high speed camera (VW-6000, KEYENCE) at frame rate of 250 fps, shutter speed of 1/2000 or 1/3000 s, and image resolution of 2.2×10^{-3} mm/pixel (Fig. 1). The camera was fixed so that the optical axis of the lens unit (VH-Z150, KEYENCE) was perpendicular to the LT surface. The field of view (FOV) of the camera was 1.4 mm × 1.1 mm (640 pixels × 480 pixels) in horizontal (L) and vertical (T) direction, respectively. The depth of field of the camera was approximately 0.05 mm. All chip formations recorded in the video clips were classified into four chip types: Type 0, I, II, or III, as defined by Franz [24, 25] and McKenzie [26], based on the appearance of chip formation. Type 0 is the flow type, Type I is the cleavage type, Type II is the shear type, and Type III is the compressive type.
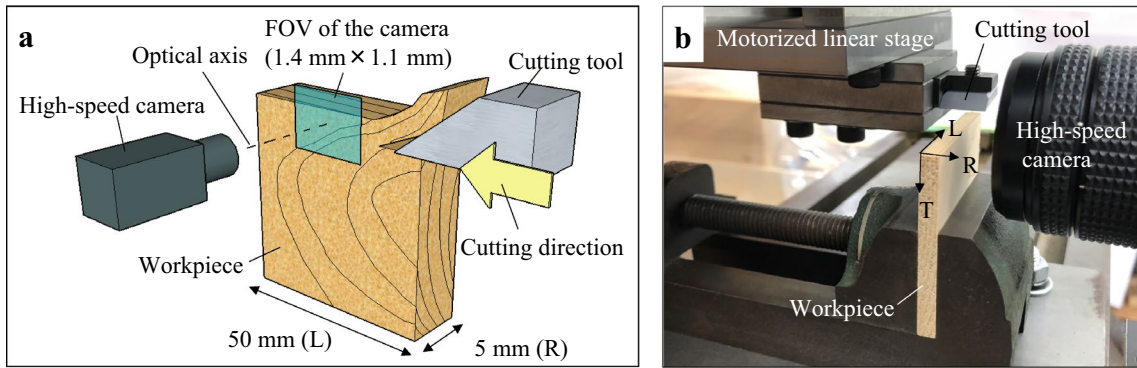
Fig. 1 The orthogonal cutting of the LR surface of the workpiece. **a** Schematic diagram of the cutting experiment and **b** picture of experimental setup

DIC analysis

Every video clip was converted into image sequence of 8-bit grayscale still images using ImageJ (ver1.50e) software [31]. The images were analyzed by the DIC program coded by us in MATLAB language [32]. A grayscale image taken before cutting and an image during the cutting process were designated as reference (un-deformed) and target (deformed) images, respectively. The region of interest (ROI) was defined in the reference image (yellow area in Fig. 2). The dimensions of the ROI were 360 pixels × 120–220 pixels (0.80 mm × 0.27–0.61 mm) in horizontal (L) and vertical (T) directions, respectively. The height of the ROI was adjusted depending on the d employed. The position of the ROI in the reference image was adjusted so that the ROI would cover the area from 90 pixels (0.2 mm) behind the cutting edge to 270

pixels (0.6 mm) ahead of the cutting edge in the target image, and the bottom of the ROI would be 110 pixels (0.24 mm) below the path of the cutting edge. The ROI was divided into a virtual grid, as shown in Fig. 2. The grid points (white squares in Fig. 2) were placed every 20 pixels (0.04 mm) in both horizontal and vertical directions inside the ROI. In the following process, the displacement of all grid points between the reference and target image could be estimated to calculate the strain distribution inside the ROI.

To search for grid points in the target image, a reference subset (red square in Fig. 2) of 21 pixels × 21 pixels centered at the grid point was set. The DIC program estimated the location of the grid point in the target image by finding the most similar target subset to the reference subset from the target image. Zero-mean normalized cross-correlation coefficient, C_{ZNCC} [16], was utilized to evaluate the similarity between the reference and target subsets:

$$C_{ZNCC} = \frac{\sum_{i=1}^{n}\sum_{j=1}^{n}\left\{F(i,j)-\overline{F}\right\}\times\left\{G(i+u,j+v)-\overline{G}\right\}}{\sqrt{\sum_{i=1}^{n}\sum_{j=1}^{n}\left\{F(i,j)-\overline{F}\right\}^2}\times\sqrt{\sum_{i=1}^{n}\sum_{j=1}^{n}\left\{G(i+u,j+v)-\overline{G}\right\}^2}}\quad(-1\le C_{ZNCC}\le 1),\qquad(1)$$

Fig. 2 Region of interest (ROI) and grid points in a reference image. The yellow area represents the ROI. The red dashed line represents the path of the cutting edge. Each white square represents a grid point. The red square represents the reference subset of the red grid point. (Color figure online)
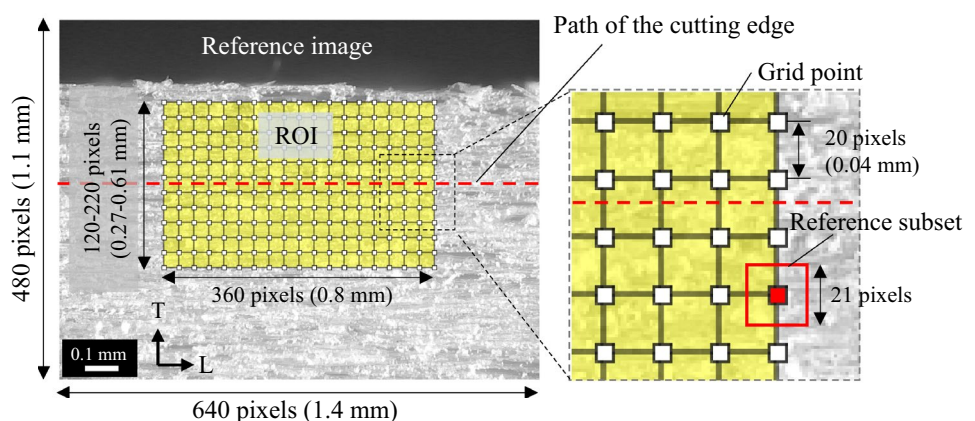
where u and v are the displacement components of the grid point in the x and y (L and T) directions between the reference and target images, respectively; $F(i, j)$ and $G(i + u, j + v)$ are the grayscale values of the pixels (i, j) and $(i + u, j + v)$ in the reference and target subsets, respectively; $\overline{F}$ and $\overline{G}$ are the averages of the grayscale values of the reference and target subsets, respectively; and n is width of the subset. Once the combination of u and v that gave the maximum C_{ZNCC} was found, the position of the grid point in the target image was determined.

After locating the grid points in the target image, as shown in Fig. 3, the strain parallel and normal to the cutting direction (L and T direction), ε_x and ε_y, respectively, and shear strain, γ_{xy}, for the area surrounded by the four neighboring grid points were, respectively, calculated using the following formulae:

were placed every 20 pixels (0.04 mm), strain in the ROI was obtained every 0.04 mm.

To estimate the displacement components, u and v, with sub-pixel level accuracy, a coarse-to-fine algorithm was utilized. The DIC program first searched for the grid point in the target image in 1 pixel steps by finding the pixel centered in the target subset, which gave the maximum C_{ZNCC}. Next, the midpoint between the pixel and each of its 8 neighboring pixels was placed virtually. The DIC program then changed the search step into 1/2 pixels and found the point that gave the maximum C_{ZNCC} from the previous pixel and its neighboring 8 midpoints. This was repeated until u and v were calculated with $(1/2)^5 \cong 3.1 \times 10^{-2}$ pixel $(6.9 \times 10^{-5}$ mm) steps. The grayscale values of the interpolated midpoint and its target subset, which were necessary for calculating C_{ZNCC}, were calculated using spline interpolation. The smallest dis-

$$\varepsilon_x = \frac{1}{2}\left[\frac{\{(x_b + u_b) - (x_a + u_a)\} - (x_b - x_a)}{(x_b - x_a)} + \frac{\{(x_d + u_d) - (x_c + u_c)\} - (x_d - x_c)}{(x_d - x_c)} \right], \tag{2}$$

$$\varepsilon_y = \frac{1}{2}\left[\frac{\{(y_a + v_a) - (y_c + v_c)\} - (y_a - y_c)}{(y_a - y_c)} + \frac{\{(y_b + v_b) - (y_d + v_d)\} - (y_b - y_d)}{(y_b - y_d)} \right], \tag{3}$$

$$\gamma_{xy} = \frac{1}{2}\left[\left\{ \frac{(y_d + v_d) - (y_c + v_c)}{(x_d + u_d) - (x_c + u_c)} + \frac{(y_b + v_b) - (y_a + v_a)}{(x_b + u_b) - (x_a + u_a)} \right\} + \left\{ \frac{(x_a + u_a) - (x_c + u_c)}{(y_a + v_a) - (y_c + v_c)} + \frac{(x_b + u_b) - (x_d + u_d)}{(y_b + v_b) - (y_d + v_d)} \right\} \right], \tag{4}$$

where x_k and y_k ($k = $ a, b, c, d) are the x and y coordinates of the four grid points in the reference image in Fig. 3, respectively; and u_k and v_k ($k = $ a, b, c, d) are the displacement components of the four grid points. Because the grid points

placement of u and v that the DIC program could measure were both $(1/2)^5$ pixels $(6.9 \times 10^{-5}$ mm), and the square element in the grid measured 20 pixels (0.04 mm), thus the smallest measureable ε_x, ε_y, and γ_{xy} of the square element were $\frac{1}{2}\left[(1/2)^5 \div 20\right] \cong 0.08\%$.

Fig. 3 Grid points in reference and target images with their x and y coordinates defined
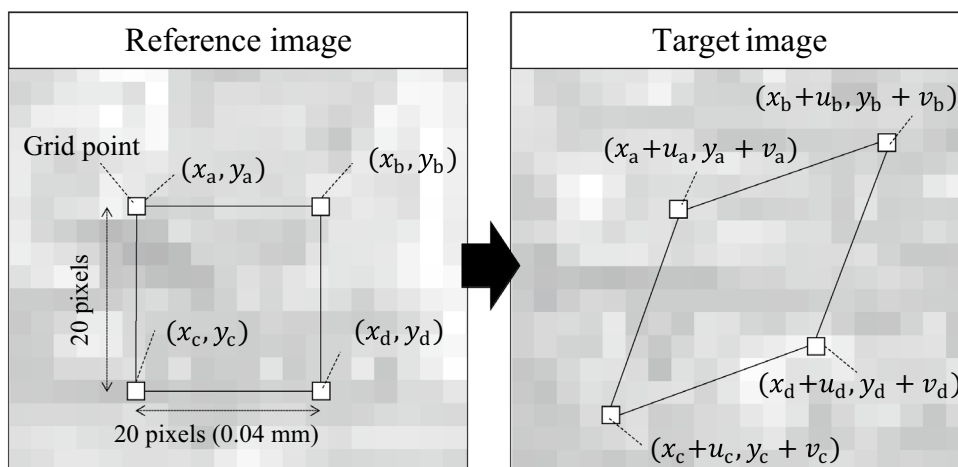
Validation tests

To confirm the precision and accuracy of the DIC program used in this study, the mean of the axial or shear strains, $\bar{\varepsilon}$ or $\bar{\gamma}$, in an artificially deformed image were calculated using the DIC program, and compared with the nominal imposed strain, ε_n or γ_n. For imposing axial strain, a reference image was compressed uniformly horizontally (L) or vertically (T) by decreasing an amount of pixels corresponding to ε_n, where the rest of the pixels were relocated by keeping their grayscale change the same as in the original image. The grayscale change was replaced by a curve using bicubic interpolation. For imposing shear strain, the reference image was sheared horizontally by sliding the pixels allocated in a horizontal line in accordance with γ_n. These processes were conducted using MATLAB [33]. The numerically deformed images were used instead of images captured by loading tests, to eliminate errors due to the fluctuation of illumination during capturing, or image distortion by optical aberration, etc. [17]. A ROI (100 pixels × 100 pixels) was placed at the center of the reference image. Grid points were placed every 20 pixels in both horizontal and vertical directions so that the ROI would be equally divided into $5 \times 5 = 25$ square elements. The mean of the strain ($\overline{\varepsilon_x}$, $\overline{\varepsilon_y}$, and $\overline{\gamma_{xy}}$), and its standard deviation (SD_ε_x, SD_ε_y, and SD_γ_{xy}), was calculated for 25 square elements, and compared with ε_n or γ_n. The coefficient of variation (CV_ε, γ), which indicates the precision of the program, and the error rate (ER_ε, γ), which indicates the accuracy of the program, were calculated using the following formulae:

$$CV\_\varepsilon = SD\_\varepsilon/\bar{\varepsilon} \times 100, \quad CV\_\gamma = SD\_\gamma/\bar{\gamma} \times 100 \ (\%), \tag{5}$$

$$ER\_\varepsilon = (\bar{\varepsilon} - \varepsilon_n)/\varepsilon_n \times 100, \quad ER\_\gamma = (\bar{\gamma} - \gamma_n)/\gamma_n \times 100 \ (\%), \tag{6}$$

Table 1 shows the results of the validation tests. The result for ε_y for $\varepsilon_n = 25\%$ is not on Table 1, because it was obvious that the displacement components of some grid points were wrongly calculated. Therefore, strain levels larger than 20% are not discussed in depth. The coefficient of variation for each type of strain seemed to decrease as ε_n (or γ_n) increased. The means of CV_ε_x, CV_ε_y, and CV_γ_{xy} among ε_n (or γ_n) were -16%, -14%, and -21%, respectively. Although ER_ε_x, ER_ε_y, and ER_γ_{xy} varied depending on ε_n (or γ_n), the means of ER_ε_x, ER_ε_y, and ER_γ_{xy} among ε_n (or γ_n) were all less than 2%. These results showed that the accuracy of the DIC program was consistently high (error rate less than 2%), although the precision was relatively low (coefficient of validation of approximately 17% on average).

Table 1 Relationships between the calculated strains (ε_x, ε_y, γ_{xy}) and the artificially imposed strains (ε_n, γ_n)

	Artificially imposed strain ε_n, γ_n (%)								Mean
	−0.94	−0.83	−1.04	−5.00	−10.00	−15.00	−20.00	−25.00	
Mean ± SD (%) (n = 25)									
$\overline{\varepsilon_x} \pm SD\_\varepsilon_x$	−0.90 ± 0.21			−4.96 ± 0.44	−10.02 ± 1.32	−14.95 ± 2.25	−19.35 ± 3.39	−24.44 ± 4.99	
$\overline{\varepsilon_y} \pm SD\_\varepsilon_y$		−0.78 ± 0.17		−5.06 ± 0.52	−10.10 ± 1.14	−14.93 ± 1.90	−20.08 ± 2.92	−25.37 ± 5.10	
$\overline{\gamma_{xy}} \pm SD\_\gamma_{xy}$			−1.00 ± 0.34	−5.07 ± 0.91	−10.12 ± 1.72	−15.17 ± 2.70	−20.22 ± 3.70		
Coefficient of variation (%)									
$CV\_\varepsilon_x = SD\_\varepsilon_x/\overline{\varepsilon_x} \times 100$	−24			−9	−13	−15	−18		−16
$CV\_\varepsilon_y = SD\_\varepsilon_y/\overline{\varepsilon_y} \times 100$		−20		−10	−11	−13	−15		−14
$CV\_\gamma_{xy} = SD\_\gamma_{xy}/\overline{\gamma_{xy}} \times 100$			−34	−18	−17	−18	−18		−21
Error rate (%)									
$ER\_\varepsilon_x = (\overline{\varepsilon_x} - \varepsilon_n)/\varepsilon_n \times 100$	−4.00			−0.81	0.16	−0.33	−3.27	−2.23	−1.75
$ER\_\varepsilon_y = (\overline{\varepsilon_y} - \varepsilon_n)/\varepsilon_n \times 100$		−6.62		1.19	0.97	−0.50	0.41	1.48	−0.91
$ER\_\gamma_{xy} = (\overline{\gamma_{xy}} - \gamma_n)/\gamma_n \times 100$			−3.99	1.53	1.17	1.10	1.12		0.40

Incremental analysis

The mean of C_{ZNCC} for all grid points, $\overline{C_{ZNCC}}$, in the validation tests decreased as ε_n increased. For instance, $\overline{C_{ZNCC}}$ when calculating ε_x decreased from 1.00 to 0.75 as ε_n increased from 0.94 to 25.00%. This suggested that when the wood undergoes high deformation, the random speckle pattern on its surface may change so greatly that the subset matching process no longer works. In such cases, the displacement components may be erroneously calculated. Therefore, incremental strain analysis was conducted in this study to measure high strain near the cutting edge. The image taken 0.02 s before the target image was selected as sub-target image. The DIC program first calculated the displacement components between the reference and sub-target image, and then the displacement components between the sub-target and target image. The two displacement components were added to get the final displacement components between the reference and target images.

Out-of-plane displacement

The cutting was conducted without bias angle, in order not to apply the lateral cutting force which may cause the out-of-plane displacement (displacement in R direction). However, when the strain in L or T direction occurs, the out-of-plane displacement may occur due to the Poisson's effect. This causes the distance from the camera to the LT surface fluctuate during the cutting. The vibration of the camera and/or the motorized linear stage may also cause the fluctuation of the distance between the camera and the LT surface. If the LT surface move outside of the depth of field of the camera, the image should be blurred. This causes the decrease of C_{ZNCC} and the DIC program should fail to track the grid points correctly. All the images analyzed by the DIC program appeared to be sharp, which indicates that the LT surface was within the depth of field. However, even if the LT surface was within the depth of field, imaginary strain should be included to the measured strain, when the distance from the camera to the LT surface has been changed between the reference and target images. Therefore, the imaginary strain due to the out-of-plane displacement was investigated.

The camera was placed at the furthest position from the workpiece where the LT surface appeared to be acceptably sharp and the reference image was taken. The camera was then moved 0.05 mm closer to the workpiece and the target image was taken. The ROI and the grid points were placed inside the reference image in the same manner with the previous validation tests, and the images were analyzed by the DIC program.

The results are shown in Table 2. The imaginary strain due to the out-of-plane displacement was so small

Table 2 The imaginary strains (ε_x, ε_y, γ_{xy}) due to the out-of-plane displacement

Mean $\pm$ SD (%) ($n=25$)	Changes in the distance from the camera to the LT surface -0.05 mm
$\overline{\varepsilon_x} \pm$ SD$\_\varepsilon_x$	0.23 ± 1.00
$\overline{\varepsilon_y} \pm$ SD$\_\varepsilon_y$	0.13 ± 0.40
$\overline{\gamma_{xy}} \pm$ SD$\_\gamma_{xy}$	$-3.7 \times 10^{-2} \pm 0.95$

compared to the strain due to the cutting. Therefore, the imaginary strain due to the out-of-plane displacement was considered to be negligible in this study.

Results and discussion

Relationships between chip type and strain distribution

Figure 4 shows examples of the distribution of the three types of strain, ε_x, ε_y, and γ_{xy}, detected near the cutting edge in Type 0, I, II, and III chip formation. The plus sign in the images represents the grid points. The square elements that include more than one grid point whose C_{ZNCC} was lower than 0.5 are not colored, because the displacement components may be erroneously calculated. The characteristics of the strain distribution for each chip type are described as follow.

Type 0 (flow type)

The first row in Fig. 4 shows an example of the distribution of three types of strain in a Type 0 chip formation ($\theta = 30°$, $d = 0.05$ mm). In Type 0 chip formation, the split of the chip occurred in the region within 0.1 mm of the cutting edge, and was hardly observed in the video clip. As a result, all three types of strain in Type 0 chip formation were smaller than those of Type I and III. However, tensile ε_y extended as the split ahead of the tool became larger because of the increase in d. Therefore, there may also be tensile ε_y distributed within 0.1 mm of the cutting edge, but the resolution of the strain distribution was not high enough to detect strain in such small area.

Type I (cleavage type)

It is already known that the cutting force periodically changes during Type I chip formation, and the force reaches its peak at the moment where the chip starts to split [25, 34].
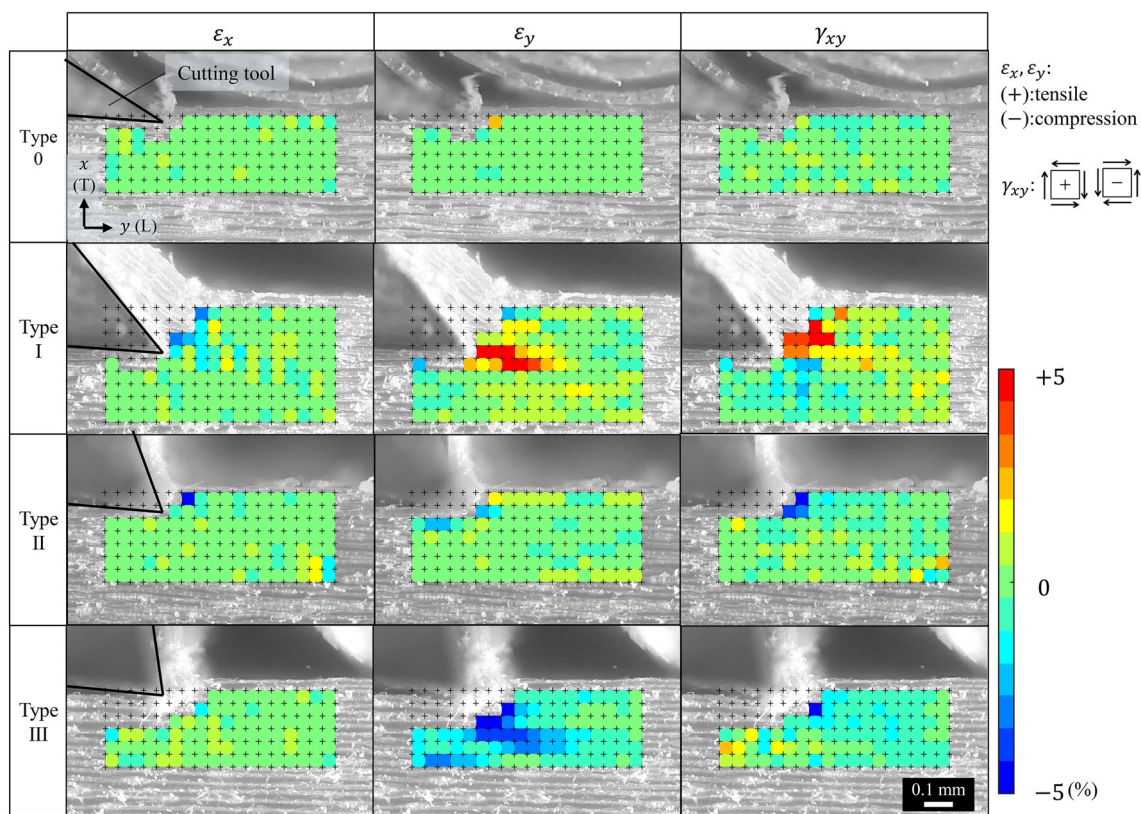
Fig. 4 The distributions of ε_x, ε_y, and γ_{xy} and their relationships to chip type. The cutting angles (θ) for Type 0, I, II, and III were 30°, 50°, 70°, and 80°, respectively. The depths of cut (d) for Type 0, I, II, and III were 0.05, 0.2, 0.1, and 0.05 mm, respectively

Therefore, the strain distribution should also change most strongly at the occurrence of the split largely, and the strain should also be at a maximum at that moment. However, the DIC program could not track the grid points placed near the path of the cutting edge after the fore-split. This was because the split of the subset was not taken into account in the DIC program, although its subset should have undergone splitting. For these reasons, the strain distribution at the moment where the chip starts to split is shown in Fig. 4.

The second row in Fig. 4 shows the strain distribution when the chip starts to split in a Type I chip formation ($\theta = 50°$, $d = 0.2$ mm). Compression ε_x was detected ahead of the tool. In an orthogonal cut, the cutting force parallel to the cutting direction was generally larger than the one normal to the cutting direction. Therefore, there was considered to be corresponding compression stress ahead of the tool, although the detected ε_x was smaller than expected. This was probably because the modulus of elasticity is larger in the cutting direction (L direction) than those in other directions. Compared with Type 0, a split originating from the cutting edge tended to travel further ahead of the tool. This cleavage ahead of the tool is often called a "fore-split". Some previous studies stated that the fore-split begin when the tensile stress in the T direction exceeded the transverse tensile strength [6,

28]. The tensile ε_y, which was detected ahead of the cutting edge seemed to cause the fore-split. In our previous studies [23, 30], the fore-split was considered to take place along the intercellular layer. Therefore, this tensile ε_y was assumed to have its peak along the intercellular layer, although it was not visible in the video clip.

The propagation of the split stopped when the chip broke down at the tip of the split in bending. Figure 5 shows the strain distribution of Type I, which was detected 0.032 s later from Fig. 4. The yellow dashed line indicates where the cutting tool was in Fig. 4. Figure 5 shows that the tensile ε_y detected along the path of the cutting edge in Fig. 4 mostly recovered after the propagation of the fore-split. On the other hand, tensile ε_y was detected near the tip of the fore-split. It was assumed that the propagation of the fore-split was caused by this tensile ε_y. The location where the chip broke down is shown by a yellow arrow in Fig. 5. Franz stated that this failure of the chip occurred when the bending stress exceeded the bending strength of the chip [25]. The compression ε_x detected in the upper side of the chip was assumed to cause the bending failure. It was assumed that the tensile ε_x would be distributed on the lower side of the chip, although the detected tensile ε_x was smaller than expected. This was probably because the compression stress
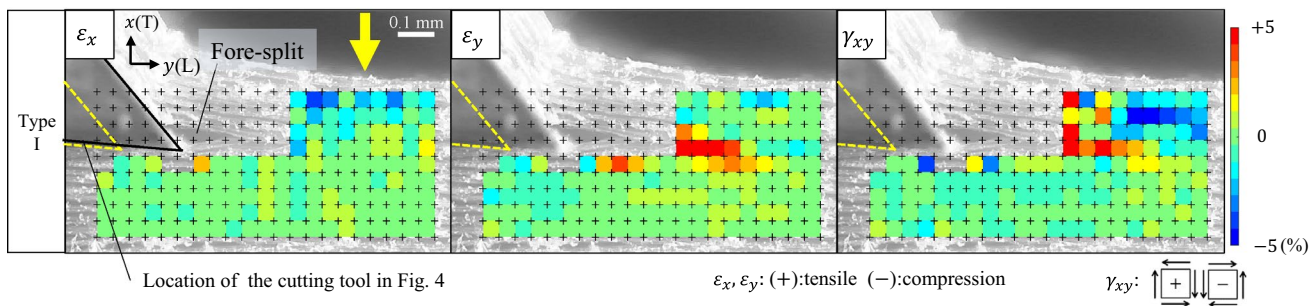
Fig. 5 Strain distribution before bending failure of a Type I chip. The image was captured 0.032 s later than the image for Type I in Fig. 4. The cutting angle (θ) and depth of cut (d) were 50° and 0.2 mm, respectively. The yellow dashed line represents where the cutting tool was in Fig. 4. The yellow arrow represents the location of the bending failure. (Color figure online)

parallel to the cutting direction related to the parallel cutting force was added to the tensile stress of the bending. After the chip broke down, the cutting edge could reach the tip of the fore-split, and the next fore-split would start again.

Positive γ_{xy} was detected above the path of the cutting edge in Fig. 4. This suggested that the cells in the chip deformed in shear along the L direction, and part of the chip might become thinner than d. As a result, it was assumed that the chip elongated in the L direction. However, it is known that the length of a Type I chip tended to be almost as same as the cutting length or even few percent shorter [33]. Figure 5 shows that negative γ_{xy} was detected where the bending failure would take place. It was suggested that this negative γ_{xy} caused the cells in the chip to shear in the T direction, and caused the chip to shorten in the L direction and to become thicker than d. As a result, some part of the chip elongated in L direction, whereas the other part shortened, resulting in the overall chip length to be almost unchanged from the cutting length.

strain ε_y might have been distributed, and the split of the chip might have occurred in that small region.

Negative γ_{xy} was detected ahead of the tool in Type II, despite the fact that positive γ_{xy} was detected ahead of the tool in Type I. This tendency could be described by considering the deformation of the chip at the cellular level and a schematic diagram of chip deformation is shown in Fig. 6. When θ was relatively small as in Type I, the cells in the chip deformed as in the left diagram in Fig. 6. As a result, part of the chip are considered to be thinner than d and longer than the cutting length, which was discussed for Type I. When θ was relatively large as in Type II, the cells in the chip tended to deform as shown on the right of the diagram in Fig. 6. As a result, negative γ_{xy} would be detected as in Fig. 4. In this case, the thickness of the chip was assumed to be thicker than d, and the length of the chip shorter than the cutting length.

Type II (shear type)

The third row in Fig. 4 shows the strain distribution in Type II chip formation ($\theta = 70°, d = 0.1$ mm). Compression ε_x was detected ahead of the tool, although the detected ε_x seemed to be smaller compared with the tensile ε_y found in Type I. However, when the anisotropy of the modulus of elasticity was taken into account as discussed earlier, the stress in the L direction in Type II might be larger than the stress in the T direction in Type I. The detected ε_y was smaller than that of Type I, and the fore-split as large as that of Type I was not observed in Type II. However, the strain distribution in the region within approximately 0.02 mm of the cutting edge was not measurable. In addition, the resolution of the image was not high enough to observe the small split of the chip in that same region. Therefore, the tensile
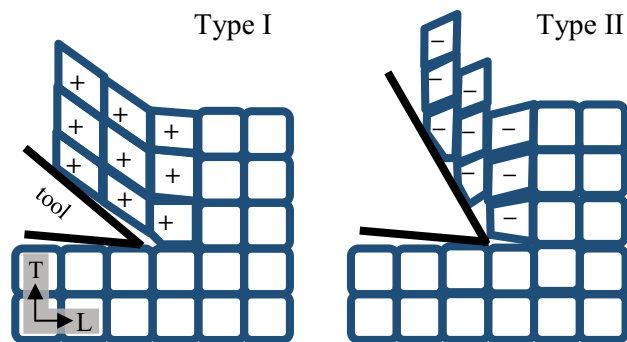
Fig. 6 Schematic diagrams of the shear strain in Types I and II. The plus and minus signs in the blue square represents the direction of γ_{xy}. (Color figure online)

Type III (compressive type)

The bottom row in Fig. 4 shows the strain distribution in Type III chip formation ($\theta = 80°, d = 0.05$ mm). The characteristics of the strain distribution in Type III were similar to those of Type II, although they could be more clearly seen in Type III. The cutting tool seemed to compress the workpiece in the T direction, thus the compression ε_y was detected beneath the cutting edge. It was considered that the deformation near the cutting edge was excessively larger than other chip types, because the region where the strain distribution was not shown because the decrease in C_{ZNCC} was wider than any other.

Relationships of ε_{y_ave} to the cutting conditions and chip type

Figures 4 and 5 suggested that ε_y near the cutting edge was greatly affected by the θ and d employed. Therefore, the relationships of ε_y to the cutting conditions and the chip type will be discussed in detail.

Cutting was conducted five times for each combination of θ and d, and five strain data for ε_y were correspondingly obtained for each combination. The mean of the five strain data of ε_y was calculated and designated as ε_{y_ave}. The distribution of ε_{y_ave} was visualized as a contour map (Fig. 7). The region where C_{ZNCC} was lower than 0.5 for more than three times out of five cuts, ε_{y_ave} was not calculated (white colored areas in the contour map in Fig. 7). The red line and black dashed line represents the original LR surface and the path of the cutting edge, respectively. Figure 7 clearly shows that the distribution of ε_{y_ave} varied according to the θ and d employed. For instance, 3% or larger tensile ε_{y_ave} tended to be detected 0.2 mm or further ahead of the tool when $\theta \leq 60°$ and $d \geq 0.1$ mm. The tensile ε_{y_ave} was distributed more widely as d increased. The distribution of tensile ε_{y_ave} seemed to be largest when $\theta = 40°$ and $d = 0.3$ mm. In this cutting condition, 5% or larger tensile ε_{y_ave} was distributed 0.3 mm ahead of the cutting edge. On the other hand, compression ε_{y_ave} tended to be detected beneath the cutting edge when $\theta \geq 70°$, regardless of d. The distribution of compression ε_{y_ave} was largest when $\theta = 80°$ and $d = 0.05$ mm; 2% or larger compression ε_{y_ave} was distributed 0.15 mm beneath of the cutting edge. This compression was not detected ahead of the cutting edge, where the chip split, but beneath the cutting edge. Therefore, this compression was assumed to be not directly related to chip formation, although this
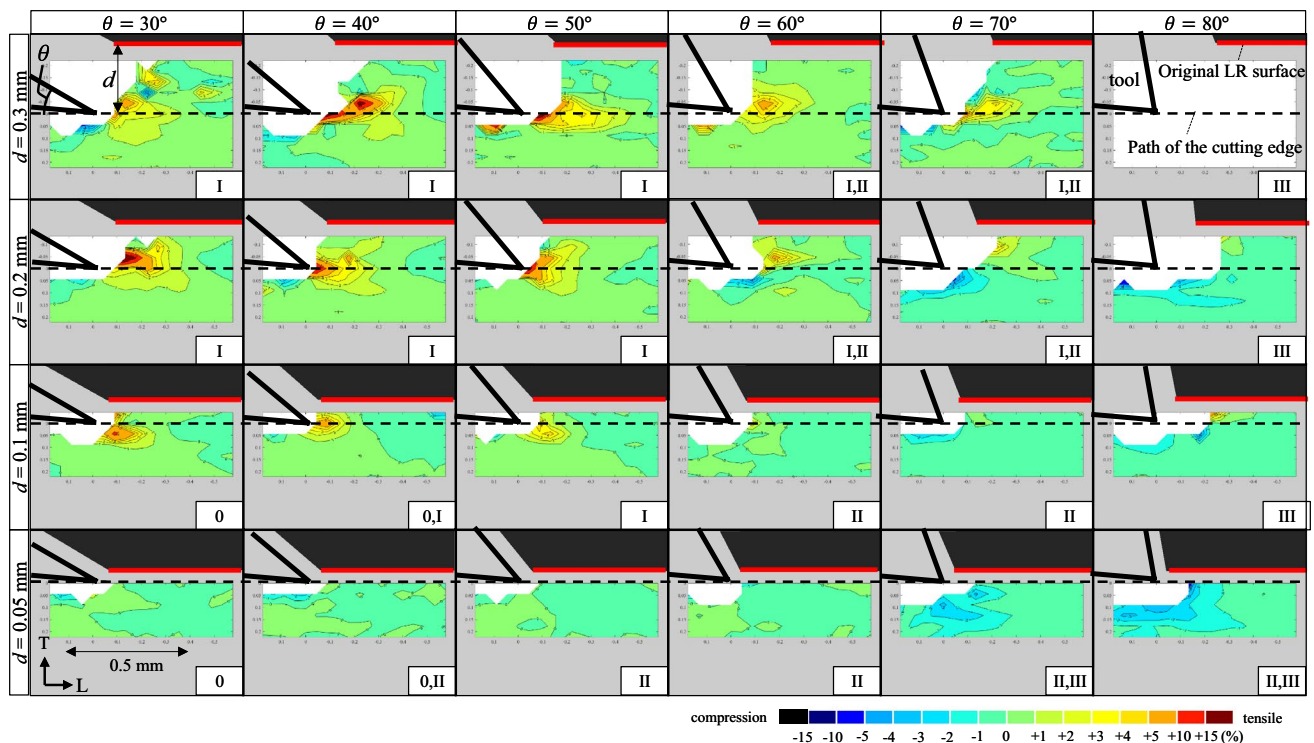
Fig. 7 Distribution of ε_{y_ave} and its relationships to cutting angle (θ) and depth of cut (d). Characters in the bottom-right corner of each contour map represent the chip type. The black horizontal dashed line and red horizontal line represent the path of the cutting edge and the original LR surface, respectively. The white area represents the area where ε_{y_ave} was not calculated because C_{ZNCC} was lower than 0.5 for more than three times out of five cuts. (Color figure online)

strain must be important from the viewpoint of surface quality, because it seemed to be related to the transverse compression of the subsurface cell layers, as discussed in our previous study [23, 30].

Figure 7 shows that the relationships of chip type occurrence to θ and d were similar to those in previous studies [25, 28, 29]. Type I was able to be characterized by the distribution of tensile ε_{y_ave} ahead of the tool, which corresponded to the occurrence of a fore-split. On the other hand, the distribution of ε_{y_ave} of Type III could be distinguished from other chip types by its compression ε_{y_ave} beneath the cutting edge. In Type 0 and II, the detected ε_{y_ave} were smaller than those in Type I or III. Their absolute value was smaller than 1%, and they were hardly distinguished from each other. The distribution of three types of strain varied depending on the chip type occurrence,

which suggested that chip formation could also be classified by the strain distribution.

Distribution of ε_{y_ave} along the path of the cutting edge

The distribution of tensile ε_y, which corresponded to fore-split occurrence, seemed to have its peak along the path of the cutting edge. To evaluate ε_y related to the split of the chip, ε_{y_ave} distributed along the path of the cutting edge (black dashed line in Fig. 7) was designated as ε_{y_path} and was plotted against the distance from the cutting edge (D) in Fig. 8. The tensile ε_{y_path} tended to increase as the cutting edge moved closer. The rate of its increase became larger as d increased. However, there were some cutting conditions in which tensile ε_{y_path} decreased as the cutting edge moved
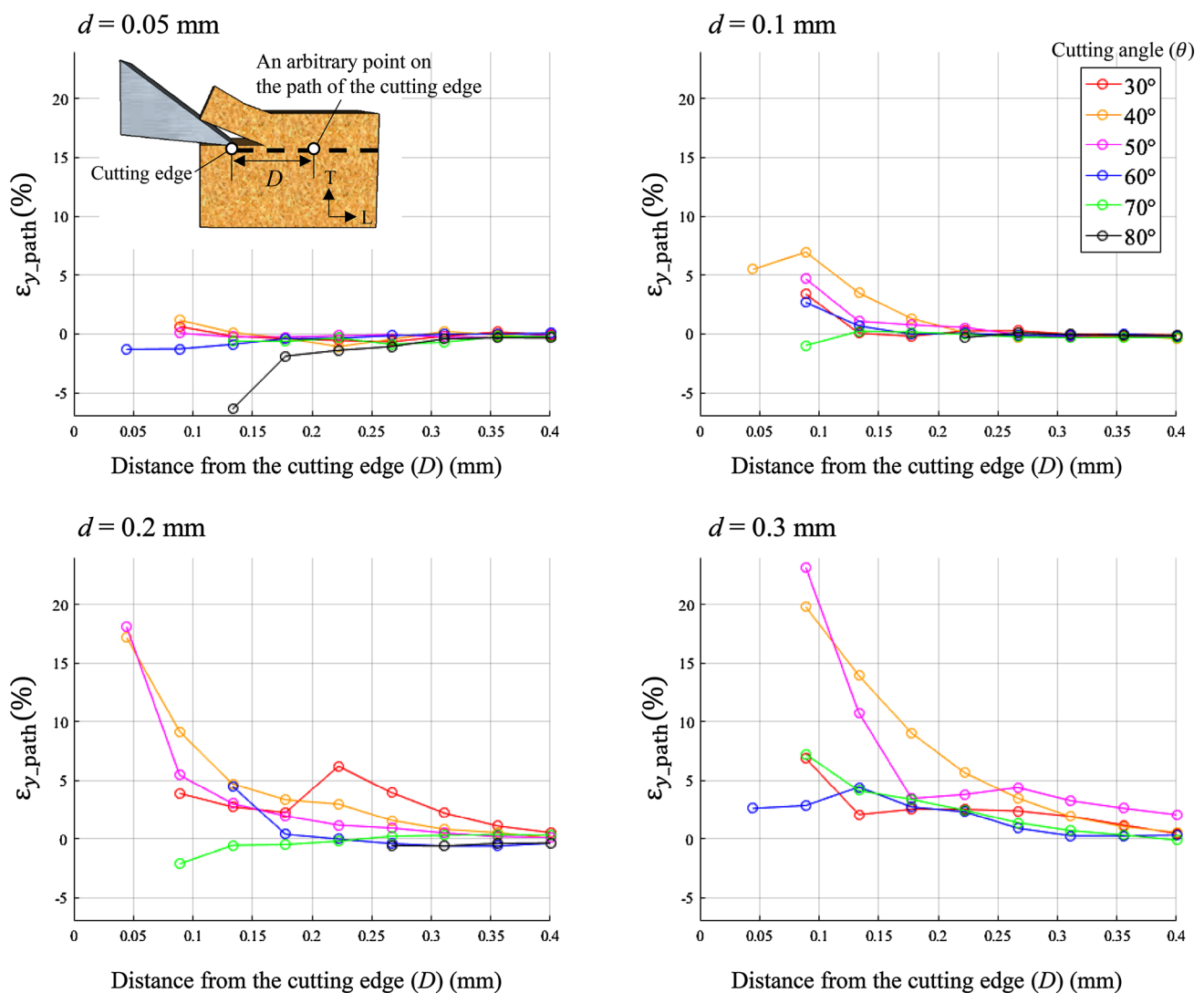
Fig. 8 Relationships of ε_{y_ave} distributed along the path of the cutting edge [ε_{y_path} (%)] to cutting angle (θ) and depth of cut (d). The color of each line graphs represents the cutting angle (θ). (Color figure online)
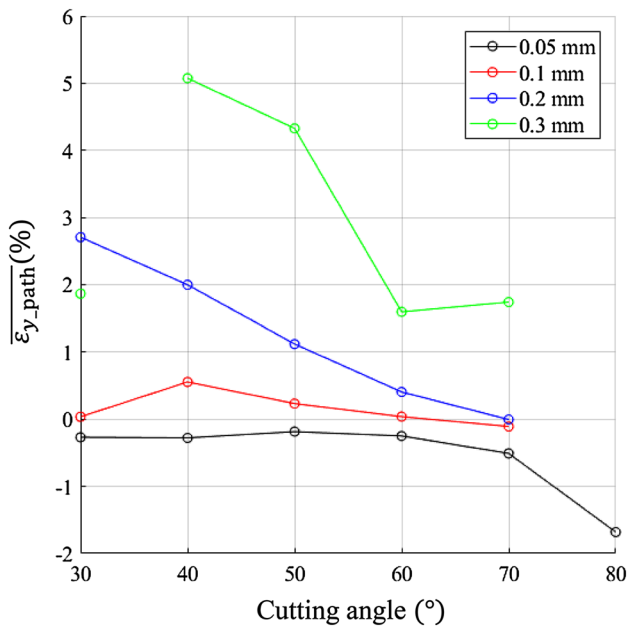
Fig. 9 Relationships of $\overline{\varepsilon_{y\_path}}$ (%) to cutting angle (θ) and depth of cut (d)

closer. This indicated that the distribution of tensile ε_{y_ave} did not always have its peak along the path of the cutting edge. This was probably because the direction of propagation of the fore-split was dependent on the fiber direction, and the fore-split did not always propagate along the path of the cutting edge [23, 31]. The value of ε_{y_path} for $D = 0.09$ mm was closest to zero when $\theta \leq 60°$, $d = 0.05$ mm. This indicated that the strain distributed only within approximately 0.1 mm from the cutting edge, and the chip formation was considered to be optimized.

To evaluate the magnitude of ε_{y_path}, the mean of ε_{y_path} for 0.13 mm $\leq D \leq$ 0.40 mm in Fig. 8 was calculated and designated as $\overline{\varepsilon_{y\_path}}$. The relationships of $\overline{\varepsilon_{y\_path}}$ to θ and d are shown in Fig. 9. When $\theta = 80°$, $d \geq 0.1$ mm, ε_{y_path} for $D = 0.13$ mm was missing, so $\overline{\varepsilon_{y\_path}}$ was not calculated. It was apparent that $\overline{\varepsilon_{y\_path}}$ decreased as θ increased, and the rate of its decrease became larger as d increased. In addition, $\overline{\varepsilon_{y\_path}}$ decreased as d decreased. When $\theta = 30°$ and $d = 0.3$ mm, $\overline{\varepsilon_{y\_path}}$ was smaller than expected. The tensile ε_y of the fore-split might have been underestimated because of the incorrect selection of the target image in which the fore-split had already occurred. By calculating $\overline{\varepsilon_{y\_path}}$, it was possible to quantify the strain distribution near the cutting edge. This indicated that the DIC method may be utilized for the evaluation of cutting conditions and machinability.

Conclusions

In this study, the quarter-sawn (LR) surface of air-dried hinoki (*Chamaecyparis obtusa*) was orthogonally cut along the grain. The LT surface during chip formation was captured using a high-speed camera, and the image was analyzed using the DIC method, to measure three types of strain, ε_x, ε_y, and γ_{xy}, distributed in the region (0.80(L) mm $\times$ 0.27 − 0.61(T) mm) near the cutting edge. The strain was measured every 0.04 mm step, and the measurable minimum and maximum strains were approximately 0.08 and 20%, respectively. The accuracy (error rate) of the DIC program was smaller than 2%, and the precision (coefficient of validation) was approximately 17%.

The three types of strain and their distribution varied greatly in accordance with the cutting condition, such as θ and d. For instance, 3% or larger tensile ε_y tended to be detected ahead of the cutting tool when $\theta \leq 60°$ and $d \geq 0.1$ mm. This tensile strain corresponded to the occurrence of a fore-split in Type I. Compression ε_y of $\geq 2\%$ tended to be detected beneath the cutting edge when $\theta \geq 70°$, regardless of d. This compression strain characterized Type III chip formation. The distribution of ε_y in Type 0 or II ($\theta \leq 60°$ and $d = 0.05$ mm) was smaller than those in Type I or III. Although there was considered to be compression stress in the L direction ahead of the tool, the distribution of ε_x was smaller than expected for almost every cutting condition employed. This was probably because of the large modulus of elasticity in the L direction. Positive γ_{xy} tended to be detected above the path of the cutting edge in Type I. Negative γ_{xy} tended to be detected ahead of the tool in Type II and III. These shear strains were considered to be related to the elongation and shrinkage of the resultant chip.

The study also found a difference in strain distribution among the chip types, and suggested the possibility of categorizing the chip formation into chip types from the strain distribution measured using the DIC method. However, the larger the modulus of elasticity was, the more difficult to detect strain using the DIC method. Therefore, we might have underestimated the stress parallel to the cutting direction, because the modulus of elasticity was larger in the L direction than in the T direction. Nevertheless, it was found to be possible to utilize the DIC method for the visualization of strain related to the deformation near the cutting edge and to chip formation.

References

1. Kinoshita N (1984) Analysis of the veneer-formation process III: analysis of cutting stress by the photo elastic coating method (in Japanese). Mokuzai Gakkaishi 30(1):32–37
2. Tochigi T, Tadokoro C (1985) Change of cutting stress in the progression of the dulling of the tool edge. Mokuzai Gakkaishi 31(11):880–887
3. McKenzie WM (1969) Applying grid patterns to wood surfaces using photosensitive lacquers. For Prod J 19(2):43–44
4. McKenzie WM, Karpovich H (1975) Measured strains in slow linear veneer cutting: effects of nosebar form and gap. Wood Sci Technol 9(3):213–231
5. Huang Y, Hayashi D (1972) Basic analysis of mechanism in wood-cutting: chip deformation in orthogonal cutting (90 – 0) (in Japanese). Mokuzai Kogyo 27(5):236–239
6. Huang Y, Hayashi D (1973) Basic analysis of mechanism in wood-cutting stress analysis in orthogonal cutting parallel to grain (in Japanese). Mokuzai Gakkaishi 19(1):7–12
7. Triboulot P, Asano I, Ohta M (1983) An application of fracture mechanics to the wood-cutting process. Mokuzai Gakkaishi 29(2):111–117
8. Tochigi T, Hayashi D (1974) Distribution of cutting stress on the rake face of the knife in veneer cutting by restricted knife-veneer contact length method (in Japanese). Mokuzai Gakkaishi (20)11:528–537
9. Sugiyama S (1974) Fundamental studies on mechanism of veneer cutting V: numerical analysis of stress distribution in workpiece during cutting without pressure bar (in Japanese). Mokuzai Gakkaishi 20(6):250–256
10. Sugiyama S (1974) Fundamental studies on mechanism of veneer cutting VI: numerical analysis of stress distribution in workpiece during cutting with sharp bar. Mokuzai Gakkaishi (in Japanese) 20(6):257–263
11. Sugiyama S (1975) Fundamental studies on mechanism of veneer cutting VII: Numerical analysis of stress distribution in workpiece during cutting without pressure bar (2) (in Japanese). Mokuzai Gakkaishi 21(1):15–21
12. Palka LC (1975) Veneer-cutting analysis by an elastic finite-element model: a case study. Wood Sci 8(2):97–104
13. Peters WH, Ranson WF (1982) Digital imaging techniques in experimental stress analysis. Opt Eng 21(3):427–431
14. Sutton MA, Wolters WJ, Peters WH, Ranson WF, McNeill SR (1983) Determination of displacements using an improved digital correlation method. Image Vis Comput 1(3):133–139
15. Sutton MA, Orteu JJ, Schreier HW (2009) Image correlation for shape, motion and deformation measurements. Basic concepts, theory and applications. Springer, New York
16. Pan B, Qian K, Xie H, Asundi A (2009) Two-dimensional digital image correlation for in-plane displacement and strain measurement: a review. Meas Sci Technol. https://doi.org/10.1088/0957-0233/20/6/062001
17. Pan B, Lu Z, Xie H (2010) Mean intensity gradient: an effective global parameter for quality assessment of the speckle patterns used in digital image correlation. Opt Lasers Eng 48:469–477
18. Choi D, Thorpe JL, Hanna RB (1991) Image analysis to measure strain in wood and paper. Wood Sci Technol 25:251–262
19. Murata K, Masuda M, Ichimaru M (1999) Analysis of radial compression behavior of wood using digital image correlation method (in Japanese). Mokuzai Gakkaishi 45(5):375–381
20. Nagai H, Murata K, Nakano T (2011) Strain analysis of lumber containing a knot during tensile failure. J Wood Sci 57:114–118
21. Keunecke D, Novosseletz K, Lanvermann C, Mannes D, Niemz P (2012) Combination of X-ray and digital image correlation for the analysis of moisture-induced strain in wood: opportunities and challenges. Eur J Wood Prod 70:407–413
22. Hellström LM, Gradin PA, Carlberg T (2008) A method for experimental investigation of the wood chipping process. Nordic Pulp Paper Res J 23(3):339–342
23. Matsuda Y, Fujiwara Y, Murata K, Fujii Y (2017) Residual strain analysis with digital image correlation method for subsurface damage evaluation of hinoki (*Chamaecyparis obtusa*) finished by slow-speed orthogonal cutting. J Wood Sci. https://doi.org/10.1007/s10086-017-1659-7
24. Franz NC (1955) Analysis of chip formation in wood machining. For Prod J 5(5):332–336
25. Franz NC (1958) An analysis of the wood-cutting process. Dissertation, University of Michigan, USA
26. McKenzie WM (1967) The basic wood cutting process. In: Proceedings of the second wood machining seminar, 10–11 Oct 1967, Richmond, pp 3–8
27. McKenzie WM, Hawkins BT (1966) Quality of near longitudinal wood surface formed by inclined cutting. For Prod J 16(7):35–38
28. Stewart HA (1971) Chip formation when orthogonally cutting wood against the grain. Wood Sci 3(4):193–203
29. Inoue H, Mori M (1979) Effects of cutting speed on chip formation and cutting resistance in cutting of wood parallel to the grain. Mokuzai Gakkaishi 25(1):22–29
30. Matsuda Y, Fujiwara Y, Fujii Y (2015) Observation of machined surface and subsurface structure of hinoki (*Chamaecyparis obtusa*) produced in slow-speed orthogonal cutting using X-ray computed tomography. J Wood Sci 61:128–135
31. Schneider CA, Rasband WS, Eliceiri KW (2012) NIH Image to ImageJ: 25 years of image analysis. Nat Methods 9:671–675
32. MATLAB Release (2017) The MathWorks, Inc., Natick, Massachusetts, USA
33. Chen X, Kimura S, Ozaki S, Yokochi H, Yonenobu H (2001) Effect of fiber orientation on chip swelling under orthogonal cutting (in Japanese). Mokuzai Gakkaishi 47(4):295–303
34. Merhar M, Bučar B (2012) Cutting force variability as a consequence of exchangeable cleavage fracture and compressive breakdown of wood tissue. Wood Sci Technol 46:965–977